Chapter 14

Alternative Approaches in Development of Heterogeneous Titania-Based Photocatalyst

Yolice P. Moreno, Cicero C. Escobar,
William L. da Silva and João H. Z. dos Santos

Additional information is available at the end of the chapter

http://dx.doi.org/10.5772/62891

Abstract

Three alternative approaches for the development of heterogeneous photocatalysts are comparatively evaluated, namely (i) the use of molecular imprinting concept for the development of heterogeneous catalysts employing rhodamine B as template and sol–gel as synthesis route; (ii) the impregnation of $TiCl_4$ on mixed nano- and micro-metric silicas, followed by calcination; (iii) the use of industrial and academic chemical residues as source of potential photocatalyst species impregnated on supports. All tests were carried on with rhodamine B as target molecule. For comparative reasons, photocatalytic tests were carried out with commercial titania (P25). The solids were characterized by nitrogen porosimetry, small-angle X-ray scattering (SAXS), zeta potential (ZP), diffuse reflectance spectroscopy in the ultraviolet region (DRS-UV), diffuse reflectance infrared Fourier transmission spectroscopy (DRIFTS), and Rutherford backscattering spectrometry (RBS). The supported catalysts resulting from silica nanoparticles and residue of the petrochemical industry achieved higher percentage of the dye degradation under ultraviolet (68.0 and 66.8%, respectively) radiation. The industrial waste reached the highest photocatalytic activity under visible (61%) radiation, while the commercial P25 achieved 82.0and 12.3% for ultraviolet and visible radiation, respectively. The textural and structural characteristics of the supported catalyst prepared with fumed silica and petrochemical waste (SiPe), namely the low-energy bandgap (1.8 eV), large surface area (280 $m^2 g^{-1}$), high pore volume (1.9 $cm^3 g^{-1}$), and high zeta potential value (−36.4 mV), may have been responsible for their high activity.

Keywords: supported photocatalyst, Rhodamine B, titania, silicas, residue, molecular imprinting

1. Introduction

Advanced oxidation processes (AOPs) are environmentally friendly technologies for the removal of organic pollutants in water and waste water. AOPs generate powerful oxidizing species, such as hydroxyl radicals ($^{\bullet}OH$, E^0 = 2.80 V) which can fragment, destroy, and degrade contaminants into small molecules (1, 2). The oxidation processes (i.e., mineralization) involve the production of CO_2, H_2O, and, eventually, inorganic ions as end products (3). The effectiveness of an AOP is proportional to its ability to generate hydroxyl radicals. This is dependent on: (i) the chemical and physical mechanisms of this technology; (ii) the nature and concentration of target contaminant; (iii) background water quality; (iv) reactor contact time; and (v) reactor configuration (3, 4).

Among the AOPs, heterogeneous photocatalysis is one of the most promising to degrade emerging contaminants and it is based on the use of bandgap semiconductors metal oxide as catalyst (3, 4). When these materials are being exposed to light with energy equal or superior than their bandgap they tend to generate electron-hole pairs which increase the number of free carriers and hence the conductivity. The ideal characteristics of a catalyst are: low raw material cost, relatively simple processing, useful temperature range, very high reaction, photochemical stability, and ability to adsorb reactants on the particle surface (3). Moreover, this method shows clear advantages, such as low cost, low toxicity, and chemical stability (5). However, once it is affected by photogenerated holes and hydroxyl radicals with a strong oxidation potential, a serious shortcoming in heterogeneous photocatalytic oxidation is the low selectivity for the most hazardous contaminants (6).

The lack of selectivity is a disadvantage, as mixtures derived from effluent streams may contain hazardous contaminants and low toxicity contaminants. In many cases, the former is present in lower concentrations, and the latter is the majority (6), but it is desirable to preferentially degrade the most toxic materials. Other drawbacks include the necessity of improving the contact between pollutant molecules and the catalyst. Regarding to this issue, the low surface area commercial catalysts, which in addition demand UV-light for the oxidative process, and UV-light in natural sunlight represents only 5–8% of the solar spectrum (7). Considering these drawbacks, alternative approaches in development of heterogeneous titania-based photocatalyst are an important issue in the topic of photocatalysis. **Table 1** illustrates recent attempts and designs of heterogeneous photocatalysts and the target molecule to which they have been tested.

As shown in **Table 1**, most of the reported systems involve the use of TiO_2 as the photocatalyst. On the other hand, the use of supports has been varied encompassing inorganic materials (silica), organic supports, ashes and, derivate from wastes. From the heterogenization point of view, sol–gel seems to be the most widely employed method, probably due to its easiness of manipulation, versatility, and broad range of potential experimental variations. The use of approaches which provide nanostructurated systems has also been reported. Phenol, drugs, pesticides, and dyes have been investigated as the target pollutant.

Catalyst system	Preparative method	Target molecule	Comments[a]	References
MI-coated photocalaysts (P25 as precursor)	Organic polimerization	2,4-Dinitro phenol	SF ranging from 1.59–3.29 for similar chlorophenols. CF ranging from 1.47 to 1.74 for similar chlorophenols. SF and CF were estimated from Kinetic experiments	(8)
MI TiO_2/WO_3 nanocomposites	Sol–gel	2-nitrophenol and 4-nitro phenol	Tetrabutyl Orthotitanate as precursor. SF ranging from 2.5 to 3.95. SF was estimated from adsorption experiments	(9)
MI based on fly-ash ceno sphere	Organic polimerization	Tetracycline	CF in ternary antibiotic solution ranging from 1.25 to 1.67. CF was estimated from Kinetic experiments	(10)
TiO_2/coconut shell powder	Acid-catalyzed sol–gel method	Carbamazepine, clofibric acid, and tri closan	Pharmaceuticals and personal care products (PPCPs) pollutants. Photocatalytic activity of the novel TiO_2–coconut shell powder (TCNSP) composite for the photodegradation of three PPCPs pollutants is investigated under UVC and black light blue UVA irradiation. Under the UVC/TCNP combination, 99% removal was achieved compared to 30% for P25	(11)
TiO_2/waste material (BEW)	Impregnation $Ti(OCH(CH_3)_2)_4$ solution was added to BEW solution	Atrazine	Synthesis of the TiO_2 nanoparticles was performed by using BEW without a reducing agent and the photocatalytic activity of the catalyst was investigated for the degradation of atrazine with UV irradiation. TiO_2 with waste material can be recycled and reused four times for the removal of atrazine. Degradation 85% after 70 min reaction	(12)
TiO_2/almond shell activated carbon	Metal organic chemical vapor deposition and impregnation	Industrial phosphoric acid solution	Load TiO_2 on the surface of active carbon by using two techniques. These photocatalysts were employed not only for the adsorption of total organic carbon (TOC) from industrial phosphoric acid solution. The catalysts showed performance higher than P25 with 90% degradation of the solution after 300 min	(13)
TiO_2/perlite granules	Metal organic chemical vapor deposition and impregnation	Ammonia	Investigate the photocatalytical activity improvement of TiO_2 (P25) powder as a photocatalyst which immobilized on perlite granules to remove ammonia from synthetic wastewater under UV irradiation	(14)
TiO_2/sand or fumed silica	Sol–gel	Nitrogen monoxide (NO)	Modification of sand and fumed silica with titania in order to obtain a photocatalytic active material for the degradation of pollutants. The sample of sand showed a high photonic	(15)

Catalyst system	Preparative method	Target molecule	Comments[a]	References
			efficiency (0.41%) comparable to that of P25 (0.40%). The coated silica fumed containing the most titania content (28 wt%) showed the best photonic efficiency (0.56%) in the degradation of NO	
TiO_2/hydroxylated fly ash ceno spheres (FACs)	Sol–gel and photoreduction method	Methylene blue (MB)	TiO_2 was coated on the surface of FACs by the sol–gel method. Platinum was then deposited on these TiO_2/FAC particles by a photoreduction method. The photocatalytic activity for the degradation of MB under visible light irradiation. Photocatalytic experiments indicated that 3 g L^{-1} of the photocatalyst (calcinated 450°C with a Pt/TiO_2 mass ratio of 1.5%) exhibited the best photocatalytic activity, as a 95% degradation of methylene blue after 8 h	(16)
TiO_2/carbon composites	Self-assembly of carbon precursors and titanium isopropoxide	Rhodamine B	Pluronic F127 was employed as a soft template. The presence of titania nanoparticles uniformly dispersed in the carbon mesostructure. Synthesis of ordered mesoporous titania–carbon composites. Under UV radiation decomposition of RhB with TiO_2/composites was (90–86%) and P25 was 50%	(17)
SnO_2/carbon nanocomposites	Solvothermal method	Rhodamine B glyphosate	Photocatalytic activity on the degradation under simulated sunlight irradiation. Uniform distribution of SnO_2 nanoparticles on the graphite-like carbon surface.	(18)
Au/TiO_2 nanocomposite	Inverse miniemulsion by sol–gel	Rhodamine B	Visible-light photocatalytic activity in the degradation of the organic dye. The Au content in the nanocomposite particles could be conveniently tuned by the amount of $HAuCl_4$ dissolved	(19)
TiO_2/catalyst residue from a Ziegler–Natta catalyst petrochemical plant	Impregnation	Drugs	Drugs, namely, atorvastatin calcium, diclofenac sodium, fluoxetine, ketoconazole, ibuprofen, dexamethasone, tioconazole, naphazoline hydrochloride, valsartan, guaifenesin, and paracetamol. The highest drug degradation was observed under UV (48.6%) and visible (45.2%) radiation with the synthesized photocatalyst	(20)

[a]Selectivity factor (SF) for single component; competitivity factor (CF) for mixture
[b]MI: molecularly imprinted

Table 1. Solid photocatalysts typically used for degradation processes.

http://dx.doi.org/10.5772/62891

In parallel, some alternative approaches in the development of potential heterogeneous photocatalyst, namely (i) the use of industrial wastes as source of photocatalyst systems which were impregnated on commercial supports (20–22); (ii) the use of the concept of molecular imprinting (MI) to afford selectivity to the adsorption and photocatalyst degradation of target molecules (23–25), and (iii) combination of nano- and micro-particles as supports (26–28) for the impregnation of titania active species were explored. Regarding to the former, the rationale was that several photocatalyst systems imply the use of metal doping to guarantee a better photocatalyst activity or to shift the spectrum of actuation toward the visible spectrum region. The employed residues (industrial petrochemical chemistry, galvanic bath residuals, silver-containing residual solutions from photography classes, metal-containing residual solutions from academic analytical chemistry classes) contained several metals (Zn, Ag, Cr, Cu Mg, including Ti) which could exhibit photocatalyst activity (29), as shown in Scheme 1.

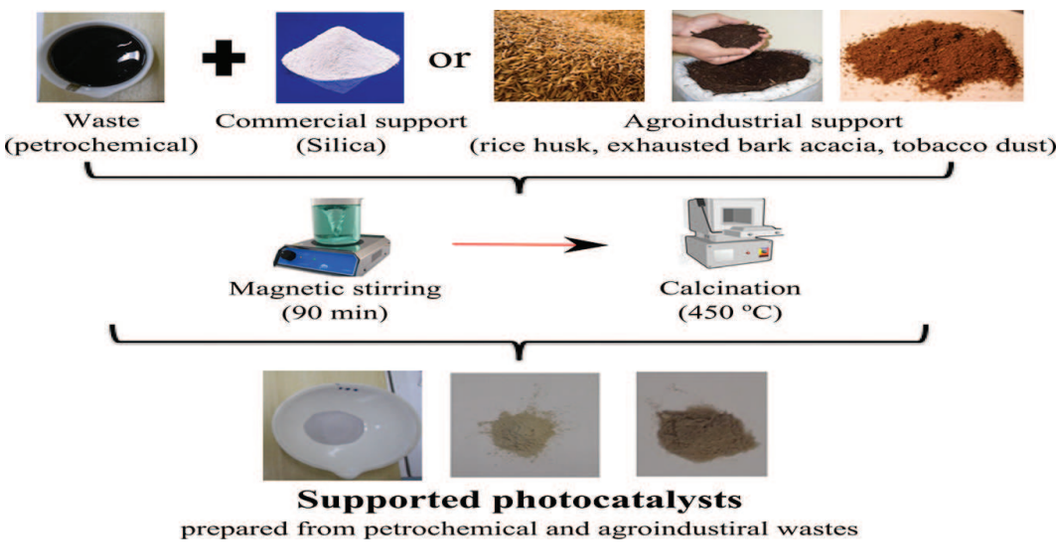

Scheme 1. Representation for the preparation of the supported photocatalysts from petrochemical and agroindustrial wastes.

In the case of MI systems, template-shaped cavities are designed using polymer matrices with memory of the template molecules that can be applied in molecular recognition (30, 31). As reported in the literature (32, 33), matrices prepared by the sol–gel method offer certain advantages compared to conventional organic polymerization methods, such as rigidity, thermal stability, tailored porosity, and flexibility in processing conditions. MI process can be roughly described in Scheme 2. At first stage, a template–functional monomer complex is assembled via appropriate interactions. A cross-linking monomer is then used to form the solid MIP matrix. Finally, the removal of the template molecule liberates an imprint cavity of a defined size and shape.

The aim of such approach is to provide a selectivity factor for heterogeneous photocatalysts, considering that the target molecule would be employed in the synthesis of the solid material. The presence of the cavities in the shape of a given pollutant would favor its adsorption and photocatalytical decomposition viz-a-viz to the other species present in the milieu.

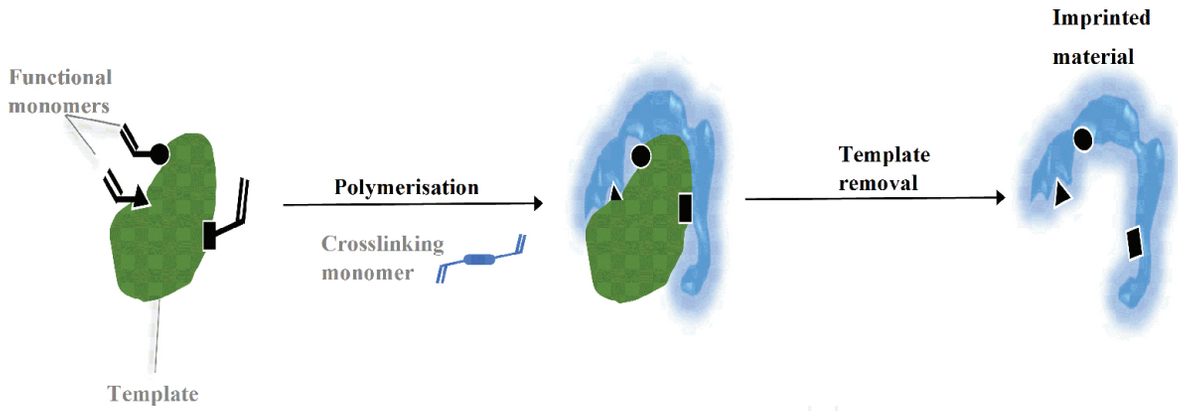

Scheme 2. Schematic representation of the imprinting process.

Concerning the third approach, nanosilicas are the materials of large surface area, bearing uniform and tunable pores, and small particle size and mechanical strength. These are important characteristics that may affect the photocatalytic activity and enhance the thermal stability of the photocatalyst. During the last decade, several mesoporous materials with different compositions of metal nanoparticles and complex nanostructured hybrid systems using SiO_2 supports have been explored for degradation of RhB by photocatalysis. For instance, core@dual–shell SiO_2–TiO_2 composite fibers (34), TiO_2/Au/SiO_2 (~50 nm) (35), Fe_3O_4@SiO_2@TiO_2@Pt (~420 nm) (36), Pt@SiO_2@TiO_2 core–shell composites (~120 nm) (37), etc. But these catalyst systems do not exhibit very large surface areas, and they may present limitations in catalyst reuse due to their size. The proposed strategy here consists in combining silica nanoparticles (7.8–12.3 nm) produced by the sol–gel method with commercial microsilica as support for $TiCl_4$ impregnation, which would be further calcinated to TiO_2 (21, 24) as shown in Scheme 3. This system offers considerable potential as solid nano-/microstructured supports for the immobilization of heterogeneous photocatalysts overcoming the size problem in the reuse, generating catalyst species both on the surface of the nanoparticle moieties, as well as on the micrometric particle (silica bulk), which improve the adsorption and the contact between the pollutant molecules and the catalyst.

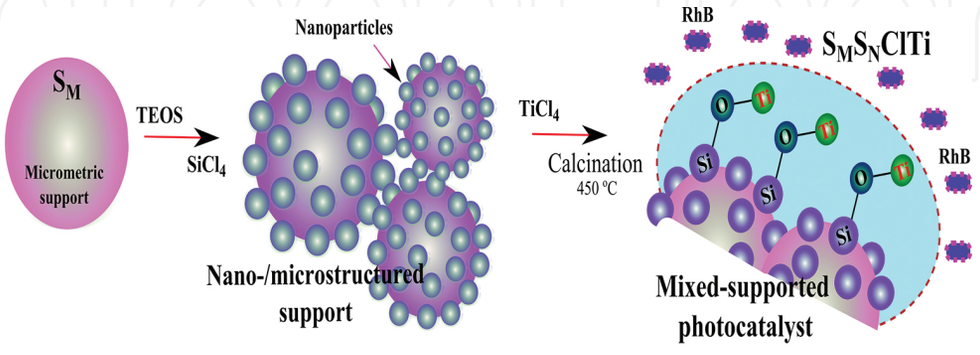

Scheme 3. Representation for preparation of mixed-supported heterogeneous photocatalyst.

http://dx.doi.org/10.5772/62891

The aim of the present manuscript is to compare the photocatalyst activity of these three above-cited approaches, operating under the same reactor conditions and with the same target molecule (Rhodamine B). For comparative reasons, commercial TiO_2 (Degussa P25) was also evaluated.

2. Experimental

2.1. Materials

Silica solutions were prepared using tetraethoxysilane (TEOS, >98%, Sigma-Aldrich) and ethanol (99.5%, Nuclear) as the solvent. Hydrochloric acid (HCl, Nuclear, 38%) and ammonium hydroxide (29%, Nuclear) solution were used as catalysts by the sol–gel method. Silicon tetrachloride ($SiCl_4$, 99%, Sigma Aldrich) was used to chemically modify the silica solutions. Sylopol-948 (Grace) was used as the micrometric silica reference. In addition, fumed silica (Wacker HDKN20), zeolite NaY (Zeolyst Internatial), and agroindustrial waste (rice husk) were used as the support for the photocatalysts. $TiCl_4$ (Merck), metal-containing residual solutions from academic analytical chemistry classes and residual Ziegler–Natta catalyst slurry (Ti-based polymerization catalyst) from a petrochemical plant were employed for the preparation of the supported titania photocatalyst. Rhodamine B ($C_{28}H_{31}N_2O_3Cl$, PrótonQuímica, P.A) was used as the dye probe for the degradation tests. Double-distilled deionized water was used for the preparation of solutions used in the catalytic tests. For comparative purposes, Degussa P25 (denoted as TiO_2) was also employed as received.

2.2. Preparation of supported photocatalysts

The molecular imprinting (MI) materials were prepared using the sol–gel process by acid route and TEOS as the raw material. Three different protocols were investigated: acid-catalyzed route 1 using $TiCl_4$ as TiO_2 precursor followed by a fast calcination (A1Ti), acid-catalyzed route 2 followed by a slow calcination (A2Ti), and acid-catalyzed route 3 using P25 as TiO_2 precursor (A3P25). All samples were prepared with 0.2 M of hydrochloric acid at a 1:2 (HCl–TEOS) ratio. For each sample, RhB was fixed at 150 mg. RhB was added to a solution of TEOS followed by addition of $TiCl_4$, and then the catalyst was added. For template removal, ultrasound-assisted (Branson-Sonifer®, Model 250) extraction was employed using methanol as the solvent (approximately 70 mL). These samples were labeled as molecularly imprinted (MI). Equivalent sample was prepared without the addition of RhB, that is, non-imprinted (NI) system (ATi). Both systems were submitted to a calcination process (450°C for 4 h at a rate of 5°C/min). In the case of system containing P25 (A3P25), this was added 2½ h after the beginning of the synthesis reaction. For comparison, the same material was synthesized without P25 (AWP25). There was no need for calcination in these systems. More details are reported elsewhere (23, 24, 38).

In the case of supported photocatalysts prepared using waste materials, 3 mL of residue was added to 1.0 g of fumed silica or zeolite NaY or rice husk. These materials were maintained

under stirring for 90 min. Then, the solution was placed in a muffle furnace for 4 h for calcination (450°C). More details are reported elsewhere (20–22).

Functionalized nanosilicas were prepared by the hydrolysis of TEOS using a standard procedure described in the literature (21, 27). Thereafter, $SiCl_4$ was added to the nanoparticles in solution. The silica nanoparticles were prepared using TEOS/$SiCl_4$ in a molar ratio of 5.0–8.0. Hereafter, the resulting nanoparticles (powder) are labeled according to the TEOS/$SiCl_4$ molar ratio employed in the synthesis. For example, S_NCl5 refers to nanosilicas prepared with a TEOS/$SiCl_4$ molar ratio equal to 5.0. Mixed-supported silicas were obtained by mixing the silica nanoparticles (previously synthesized) with 0.2 g of a Sylopol-948 (commercial micrometric silica (S_M)) and stirred for 3 h. Mixed silicas were labeled as S_MS_NCl, indicating the presence of Sylopol-948 (S_M) combined with synthesized nanosilicas (S_NCl) from the preparation with $SiCl_4$. Further details are reported elsewhere (27). 3.0 mL of $TiCl_4$ was added to 1.0 g of synthesized silica particles and stirred for 90 min. After, the samples were then placed in a muffle furnace for 4 h for calcination (450°C). Two different nanometric supports were used in the production of nanometric catalysts (labeled S_NCl5Ti to S_NCl8Ti), and mixed silicas were used in the production of two mixed support catalysts (S_MS_NCl5Ti to S_MS_NCl8Ti).

Scheme 4 depicts the steps involved in the preparation of each supported photocatalyst as well as the corresponding labels. Preparation of MI materials is illustrated in Scheme 4a, b. Synthesis of functionalized nanosilicas catalysts and mixed-supported silicas ones is shown in Scheme 4e, d. Scheme 4e displays the preparation of catalysts using industrial and academics waste as the source of photocatalysts as well as the corresponding employed labels.

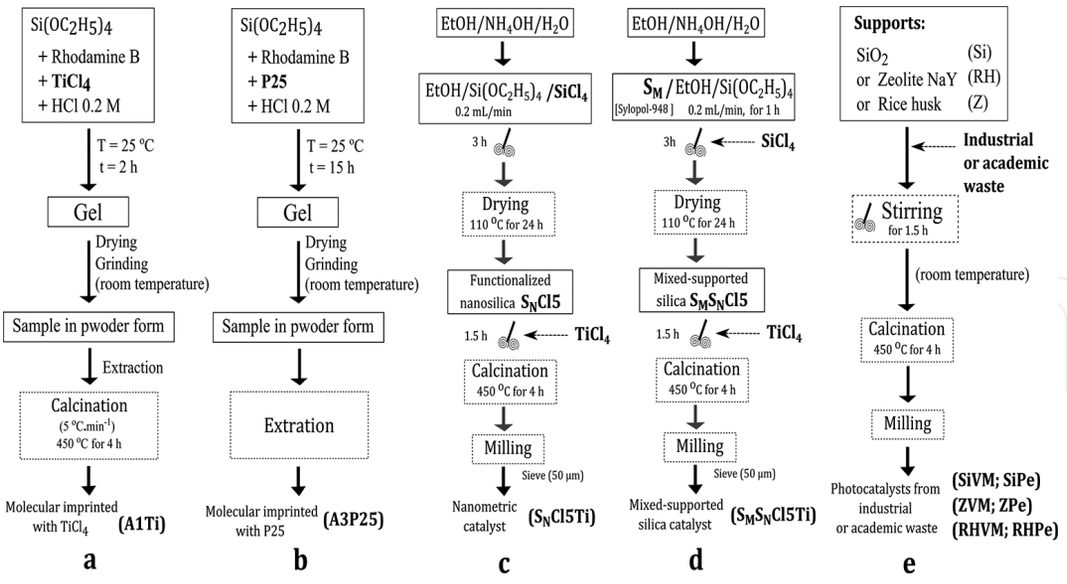

Scheme 4. Steps employed for preparation of the supported titania photocatalysts from MI materials (a, b), nanosilicas (c), mixed silicas (d), and fumed silicas or zeolite or rice husk (e).

Table 2 presents the set of photocatalyst compared in the present study, as well as the corresponding label.

Method	System	Label
	Degussa P25	**P25**
	Photolysis	**PHOTO**
Molecular imprinted (MI)	$TiCl_4$ + RhB	**A1Ti**
	$TiCl_4$ + RhB	**A2Ti**
	P25 + RhB	**A3P25**
	RhB	**A4WP25**
	$TiCl_4$	**ATi**
Nanoparticles and mixed silicas	$TiCl_4$ + S_M	**S_MTi**
	$TiCl_4$ + S_NCl5	**S_NCl5Ti**
	$TiCl_4$ + S_NCl8	**S_NCl8Ti**
	$TiCl_4$ + S_MS_NCl5	**S_MS_NCl5Ti**
	$TiCl_4$ + S_MS_NCl8	**S_MS_NCl8Ti**
Industrial and academic wastes	Various metals + SiO_2	**SiVM**
	Petrochemical + SiO_2	**SiPe**
	Various metals + Zeolite NaY	**ZVM**
	Petrochemical + Zeolite NaY	**ZPe**
	Various metals + Rice husk	**RHVM**
	Petrochemical + Rice husk	**RHPe**

Table 2. Supported photocatalysts prepared from MI materials, synthesized silica particles, and chemical waste.

2.3. Characterization of the supported titania photocatalysts

The specific surface area (S_{BET}), the pore diameter (Dp_{BJH}), and pore volume (Vp_{BJH}) were calculated by the Brunauer-Emmett-Teller method (BET) (39) and Barrett-Joyner-Halenda (BJH) algorithm (40), respectively. Measurements were taken using a Micromeretics TriStar II 3020 in the partial pressure range of $0.01 < P\,P_0^{-1} < 0.95$. Small-angle X-ray scattering (SAXS) measurements were performed at the SAXS1 beamline at the National Synchrotron Light Laboratory (LNLS), Campinas, Brazil. The scattered X-ray beam presenting a wavelength (λ) of 1.488 Å was detected on a Pilatus 300 k detector (27). I(q) vs. q scattering profiles were fit by multi-level of structural organization using the Beaucage model (41–43) in the Irena routine (44). The zeta potential of the nanoparticles and mixed supports (approximately 250 mg) was measured using Zetamaster equipment (Malvern Instrument). Metal content in the catalysts was determined by Rutherford backscattering spectrometry (RBS) using a He^{2+} beam of 2.0 MeV incident on the homogeneous tablets of the compressed (12 MPa) catalyst powder. SEM images were collected at the Center for Nanoscience and Nanotechnology (CNANO, UFRGS) in an EVO-50 (Carl Zeiss, Inc.) field emission scanning electron microscope equipped with a secondary electron detector Everhart-Thornley (ETSE) at 0.2–30 kV and with a working distance of 14 mm. UV–vis spectra of the supported photocatalysts in powder form were

recorded using a Varian Cary 100 Scan Spectrophotometer with an accessory DRA-CA-301 (Labsphere) in the diffuse reflectance mode by co-adding 32 scans in the 200–800 nm range. The energy bandgap was determined by means of the Kubelka–Munk function. Scans ranged from 200 to 800 nm. Scanning electron microscopy (SEM) and energy dispersive X-ray (EDX) were performed using a JSM5800 (JEOL) microscope, operating between 5 and 20 kV. The samples were coated with a thin layer of conductive carbon by a sputtering technique. Diffuse reflectance infrared Fourier transmission spectroscopy (DRIFTS) was carried out at room temperature in a Bomem MB-102 spectrometer equipped with a diffuse reflectance accessory. Analyses at the absorbance modes were performed by co-adding 32 scans with 4 cm^{-1} of resolution. The spectral characteristic bands of the harmonic vibration of the silica materials network [$\nu_{as(Si\text{-}O(\text{-}Si))}$] [$\nu_{as(Si\text{-}O(\text{-}Si))}$] were studied by the FT-IR spectra in the region of 1300–1000 cm^{-1} (45–47). The broadband between 1300–1000 cm^{-1} was deconvoluted via Gaussian functions into four independent components: two (TO_4 and TO_6) associated with the transverse-optic (TO) modes and two (LO_4 and LO_6) with the longitudinal-optic (LO) modes of Si-O-Si using a nonlinear least-squares fitting method [39]. The percentage of sixfold rings (SiO_6) in the silica network (Q_6) was estimated using the following ratio of fitted areas (27, 48, 49):

$$\%(\mathrm{SiO_6}) = \frac{[A(LO_6) + A(TO_6)]}{[A(LO_6) + A(TO_6) + A(LO_4) + A(TO_4)]} \times 100 \quad (1)$$

2.4. Statistical analysis

The SPSS Statistical software (SPSS for Windows, version 19, IBM®) was used to analyze the relationships among the data. All statistical tests were performed at the $P < 0.05$ level of significance. The Spearman correlation coefficient (r_{Sp}) was used as a nonparametric measure of statistical dependence between two variables.

2.5. Photocatalyst tests

For tests with the Rhodamine B, 0.0175 g of catalyst was added to 25 mL of the test molecule (20 mg L^{-1}) at pH of the reaction medium (pH ≅ 4.3). The solution was then transferred to the reactor, and after adjusting the temperature (at 30°C), the lamp was switched on to start the irradiation. During each experiment, circulation of suspension was maintained to keep it homogenous and to have uniform temperature. Samples (5 mL) were taken at regular time intervals (0, 5, 15, 30, and 60 min) and then centrifuged (Cientec CT-5000R) for 20 min at 5000 rpm in order to separate the catalyst particles from the samples. To determine the concentration of RhB, solution absorbance was read in a Varian Cary 100 UV–vis spectrophotometer at the wavelength of maximum absorbance of target molecule (553 nm for RhB), and the absorbance was related to the concentration of the RhB through a calibration curve: Abs = 0.2053 C (mg L^{-1}) ($R^2 = 0.9911$; N = 7). All photocatalytic tests were performed in duplicate (error value lower than 5%). Photolysis tests were also performed to determine the percentage of dye degradation due to UV light exposure without the presence of a photocatalyst.

3. Results and discussion

According to the RBS results, the metal concentration is low in terms of the Ti/Si ratio. Systems S_MS_NClTi showed a Ti average composition of 0.45 wt%/SiO_2, whereas the S_NClTi obtained 1.33 wt%/SiO_2. Therefore, the S_N5ClTi achieved a higher metal content. According to the SEM-EDX results, the average atomic percentage of Ti was 16.04 ± 3.05 at.%. As shown in **Table 3**, Si was present in all the samples. Depending on the photocatalysts from wastes, Cu, Zn, Al, Ti, Cr, or Mg were also present.

System	C/Si	Cu/Si	Zn/Si	Al/Si	Ti/Si	Cr/Si	Mg/Si
SiVM	1.03	0.05	0.01	0.13	0.01	0.01	–
SiTi	4.55	0.04	–	–	0.52	–	2.11
ZVM	–	0.01	0.01	0.67	0.01	0.01	–
ZPe	–	0.02	–	0.67	0.35	–	0.08
RHVM	7.60	0.01	0.01	–	0.02	0.01	0.01
RHPe	7.60	0.01	–	–	0.04	–	0.04

Table 3. The chemical composition of the catalysts in terms of atomic ratio determined by SEM-EDX, considering Si as internal standard.

Photocatalyst activity in the degradation of rhodamine B was comparatively evaluated by the three supported catalyst systems, under UV and visible irradiation, as shown in **Table 4**.

As shown in **Table 4**, the efficiency of the photolysis degradation was <8%. The P25 showed an excellent performance in the UV (82%), but poor performance in the visible (12.3%). All of the supported titania photocatalysts exhibited better photocatalyst activity (25.4–61.6%) for RhB degradation than commercial P25 under visible radiation. The S_NCl5Ti catalyst showed the best photocatalyst activity under UV (68%) irradiation, followed by SiPe (66.8%).

The approach of nanometric photocatalysts showed better performance (59–68%) than the nano-micrometer systems (33.6–42.7%) under UV and visible radiation. This is due to the incorporation of higher amount of titanium on the surface of nano-catalysts, as shown in the results of RBS. However, both approaches are valid for the degradation of organic pollutants from supports such as silicas synthesized by sol–gel, because nano-micrometer photocatalysts (25.4–30.1%) also were better than the P25 under visible radiation. The advantage of a nano-micrometric system resides in the possibility of reusing the catalyst several times as have already studied (27, 28, 50), which is a current limitation of nanoscale catalysts.

All the supported photocatalysts from industrial waste exhibited photocatalyst activity in dye degradation, although with catalyst activity lower than that of Degussa P25 under UV radiation. On the other hand, all the catalysts from industrial and academic wastes exhibited activity higher than that of Degussa P25 under visible radiation, suggesting a potential

application of such photocatalysts under sun irradiation. Among them, the SiPe catalyst showed the best photocatalyst activity under UV (66.8) and visible (61.6%) irradiation. The higher efficiency in the photocatalytic activity of the SiPe sample compared with the other samples may be because the SiPe sample has the lowest Eg value, the largest ZP value (in the module), and the highest S_{BET} (available surface area of the active sites) and Vp values.

Method	System	Degradation RhB (%) radiation	
		UV	Visible
	P25[a]	82.0	12.3
	P25[b]	44.3	n.d.
	Photo	5.5	n.d.
Molecular imprinted (MI)	**A1Ti**	32.2	n.d.
	A2Ti	37.8	n.d.
	A3P25	50.9	n.d.
	A4WP25	20.0	n.d.
	ATi (NI)	12.7	n.d.
Nanoparticles and mixed silicas	**S_MTi**	n.d	n.d.
	S_NCl5Ti	68.0	45.1
	$S_M S_N$Cl5Ti	42.7	30.1
	S_NCl8Ti	59.0	35.6
	$S_M S_N$Cl8Ti	33.6	25.4
Photocatalysts from wastes	**SiVM**	41.1	48.2
	SiPe	66.8	61.6
	ZVM	31.7	30.7
	ZPe	53.0	46.3
	RHVM	27.8	11.2
	RHPe	30.9	30.6

[a]Experimental WL; catalyst = 0.7 g L^{-1}, CRhB = 20 mg L^{-1}, T = 30°C, natural pH = 4.3, UV radiation of 30 W m^{-2}, and visible of 202 W m^{-2} error of 5%.
[b]Experimental conditions: catalyst = 0.55 g L^{-1}, CRhB = 20 mg L^{-1}, T= 30°C, natural pH, UV radiation of 30 W m^{-2}, and error of 5%.

Table 4. Percentage degradation of RhB under visible (a) and UV (b) irradiation after 60 min of reaction.

We have shown that our MI systems showed selectivity and competitiveness up to 1.9 and 3.5, respectively, toward RhB. Also, compared to the commercial sample (P25), selectivity (up to 180%) and competitiveness (up to 290%) were obtained (24). However, the average of activities under UV radiation was lower than the average values obtained by nano-silica (1.44-fold

lower) and industrial wastes routes (1.16-fold lower). On the other hand, the lowest value of activity achieved within the MI systems containing TiO_2 (32.2%) was comparable to the S_MS_NC18Ti (33.6%) and higher than RHVM (27.8%), which showed the lowest activities within nanosilica and industrial wastes routes, respectively. Despite their lower activities, one of the main advantages of MI approach is the possibility to achieve better selectivity removal compared to the commercial samples and also reusability (51), which are recognized drawbacks in heterogeneous photocatalysis (6). **Figure 1** shows the results of RhB photocatalyst decomposition under visible and UV radiation by selected photocatalysts from each of the three approaches.

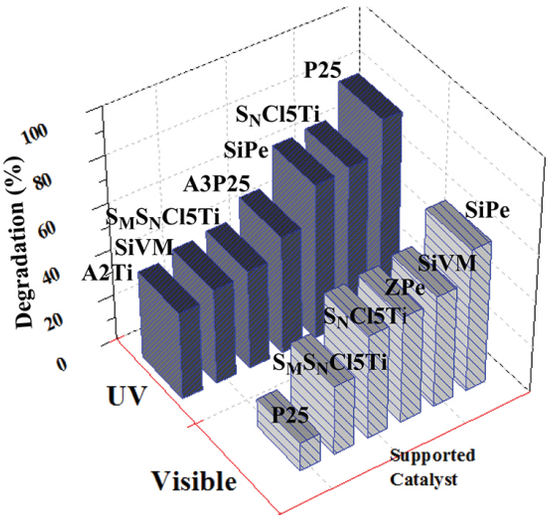

Figure 1. Percentage of degradation of RhB under visible (a) and UV (b) irradiation after 60 min of reaction by better photocatalysts each approaches.

As shown in **Figure 1**, comparing among all the supported photocatalysts, the performance of P25 is inverted under visible radiation, becoming the lowest among all. The catalysts from industrial waste dominate over nanosilicasand mixed silicas supports.

In order to understand the differences concerning each alternative route, these systems were characterized by a series of complementary techniques aiming at accessing some information concerning textural, structural, and morphological aspects of these supported catalysts.

3.1. Textural characteristics of photocatalysts

The catalytic activity of the particle samples is proportional to their specific surface area because it requires the adsorption of reactants and also the transfer of photoexcited electrons into the adsorbed molecules, which is directly related to the diffusion of the RhB to the catalyst center (52). The specific surface area (S_{BET}), the specific pore volume (Vp_{BJH}), pore diameter (Dp_{BJH}) are presented in **Table 5**.

Method	System	S_{BET} ($m^2\ g^{-1}$)	Vp_{BJH} ($cm^3\ g^{-1}$)	Dp_{BJH} (nm)	Rg (nm)	P	ZP (mV)	Eg (eV)	SiO_6 [e] (%)
	P25	56.0	0.22	2.6	1.4	4.0	−3.6	3.3	n.d.
Molecular imprinted (MI)	**A1Ti**	634.5	0.47	3.1	9.8	3.4	−22.9	2.1	48.7
	A2Ti	750.6	0.40	2.9	9.8	3.6	−10.9	2.0	54.9
	A3P25	516.4	0.25	2.7	7.5	3.3	−21.9	2.8	60.0
	A4WP25	837.8	0.42	2.3	1.0	3.7	−10.6	n.d.	52.0
	ATi (NI)	463.4	0.30	2.9	4.3[c]	3.3[d]	−29.3	2.2	41.0
Nanoparticles and mixed silicas	**S_MTi**	240.9	0.10	3.0	4.2	4.0	−8.4	3.8	37.2
	S_NCl5Ti	123.6	0.01	2.9	6.8	2.5	−29.5	2.8	50.3
	S_MS_NCl5Ti	155.8	0.09	4.3	12.3	2.0	−21.9	3.1	31.4
	S_NCl8Ti	107.1	0.16	9.1	7.8	3.6	−26.5	3.0	88.7
	S_MS_NCl8Ti	109.8	0.17	8.4	8.6	3.6	−10.8	3.7	74.7
Photocatalysts from wastes	**SiVM**	277.0	0.4	12.1	6.2	3.9	−22.3	2.7	n.d.
	SiPe	280.0	1.9	20.1	2.7	3.9	−36.4	1.8	n.d.
	ZVM	156.0	0.3	0.6	2.4	4.0	−26.4	2.9	n.d.
	ZPe	272.0	0.3	0.7	2.6	4.0	−27.6	2.3	n.d.
	RHVM	118.0	0.5	1.3	3.1	4.0	−20.3	3.2	n.d.
	RHPe	182.0	0.5	8.0	0.6	4.0	−28.6	2.9	n.d.

[a]Extracted from high-q region (SAXS);
[b]Power-law decay (P) extracted from low-q region (SAXS);
[c,d]These systems showed a structure that consists of two organizational levels;
[e]%$(SiO)_6$ was determined by Eq. (1).

Table 5. BET isotherm parameters, radius of gyration of particles (Rg), and the linear Power-law decay (P) obtained through unified fit on the SAXS profiles, zeta potential (ZP), bandgap energy (Eg), and percentage of sixfold rings (SiO_6) for the photocatalysts.

According to **Table 5**, all systems prepared are mesoporous materials as classified by the International Union of Pure and Applied Chemistry (IUPAC) (53, 54). It can be seen that all systems have shown values of surface area higher than the commercial sample. Also, the mean value achieved for the MI systems is ca. 4.6-fold and 3.1-fold higher than the mean values found for nanometric and photochemical residue, respectively. Moreover, the supported photocatalysts with $TiCl_4$ showed a reduction in the final surface area in relation to the nanometric and mixed supports, which also are observed in photocatalysts prepared with petrochemical residue and solution of various metals supported on zeolite NaY (ZVM and

ZPe) and the system with molecular imprinted in which P25 was added (A3P25). This fact can be due to the high calcination temperature providing the agglomeration of the catalytic metal particles, thus decreasing the available surface area (55, 56) and the degree of structural organization and internal pores between nanoparticles, mixed silicas, and zeolite NaY (27, 56). Considering the resulting heterogeneous photocatalysts from $TiCl_4$ or wastes impregnation, the SiPe reached the highest specific surface area and pore volume. This increase can be associated with action of the waste or $TiCl_4$ on the respective support rendering difficult the contact between the particles and avoiding the agglomeration of the catalytic particles.

3.2. Multi-scale organization of the photocatalysts analyzed by SAXS

The photocatalysts were further analyzed by SAXS, which provides structural information, that is, a broader and clearer view of catalysts formation and aggregation (57). The multi-hierarchical organization of these materials, their gyration radius (Rg), and fractal structure (P) were investigated through the Unified approach (41–43) in the Guinier and Power-law regions. Table 5 shown radius of gyration of particles (Rg) and the linear Power-law decay (P), obtained through Unified fit on SAXS profiles of photocatalysts.

As shown in Table 5, photocatalysts are organized into three levels, excepting ATI and P25 which show two levels. Rg results show that the primary particle size ranges from 0.6 to 12.3 nm, according to the preparation method. Catalysts S_MS_NCl5Ti was the largest particle, due to the combination of nanoparticles incorporated into the surface of a micrometric support as (S_M), resulting in bigger aggregated mixed silica catalyst (S_MS_NClTi).

Comparing fractal structure (P) results, P25 is a completely spherical particle, as well as the photocatalyst from industrial wastes (P = 4), which corresponds to spherical and dense clusters of approximately smooth surface according to Beaucage (42, 43). On the other hand, all MI systems showed fractal surface ($3.3 < P < 3.7$), whereas that nano- and micronano-photocatalysts mass fractals ($2.0 < P < 2.5$) to surface fractals aggregates ($P = 3.6$).

3.3. Zeta potential (ZP) measurements

Zeta potential (ZP) measurements were used to verify the stability of the suspensions of the studied systems, to determine its influence on the RhB dye adsorption of the supported photocatalysts and to correlate the electric potential information with the results obtained by SAXS. Table 5 shown the ZP and E_g values. **Figure 2** shows the relationship among S_{BET}, Rg and ZP of the best catalysts for each strategy discussed in this article.

The supported catalysts using the MI approach present ZP between −10.6 and −22.9 mV and in the case of synthesized nanoparticles and mixed silicas, ZP lies between −10.8 and −29.5 mV. For the impregnated with industrial and academic wastes ZP was between −20.3 and −36.4 mV (as shown in Table 5).

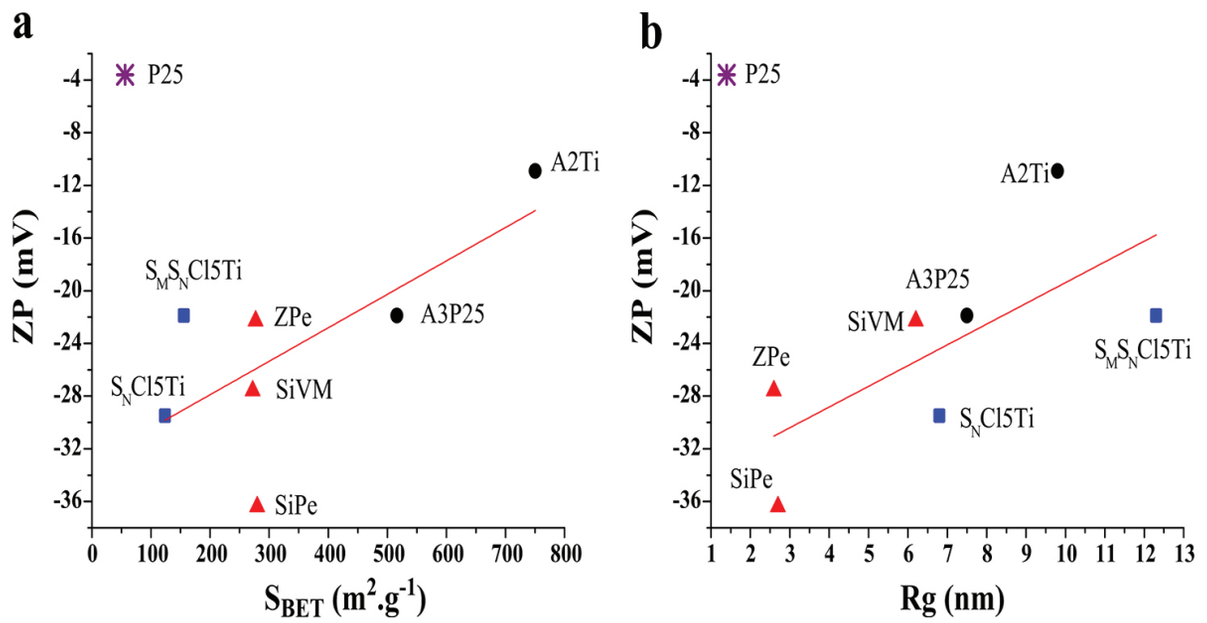

Figure 2. The zeta potential of better photocatalyst dispersions as a function of (a) S_{BET} and Rg by SAXS. Spearman's correlations: $r_{Sp} > 0.705$ for (a) and $r_{Sp} > 0.757$ for (b).

According to **Figure 2a**, there is a direct correlation ($r_{Sp} > 0.705$) between electronic (ZP) and textural properties (SBET) of photocatalysts. Among all the photocatalysts, SiPe showed the highest ZP (−36.4 mV) (in module) and all systems bear a negative charge on their surfaces. The negative charge density on the surface is greater in the smaller photocatalyst, most likely due to the smaller particle size (2.4–6.8 nm). It is worth noting that high surface area supports are desirable for photocatalysis because it can promote the adsorption of the dye RhB to be degraded on the catalyst/support surface (21). Such behavior is in accordance with the results of Ribeiro et al. (58) and Gaya and Abdullah (59), who reported that the performance of a photocatalyst is dependent on the surface textural characteristics (size, surface area, and pore volume) because the local morphology strongly influences the number of striking photons and the rate of the photocatalytic reaction.

Conversely, it was possible to observe a strong direct correlation ($r_{Sp} > 0.757$) between the zeta potential and the particle radius supported catalysts, as shown in **Figure 2b**. A smaller particle size corresponds to a higher negative surface charge: The nanometric photocatalyst (SiPe, ZP = −36.4 mV and Rg = 2.7 nm) exhibited this trend. The preparation of photocatalyst by impregnation with industrial and academic waste showed two effects: (i) increase the particle radius (Rp) and (ii) enhance the negative zeta potential. In this study, better photocatalyst showed an increase in zeta potential as the particle radius increased (−10.9 to −36.4 mV). The trend is consistent with the fact that the van der Waals forces are dominant over the electrostatic repulsive ones: the electrical double-layer thickness decreases, thereby promoting the agglomeration of primary particles, which in turn affords the particle growth size, as shown in the SAXS analyses.

http://dx.doi.org/10.5772/62891

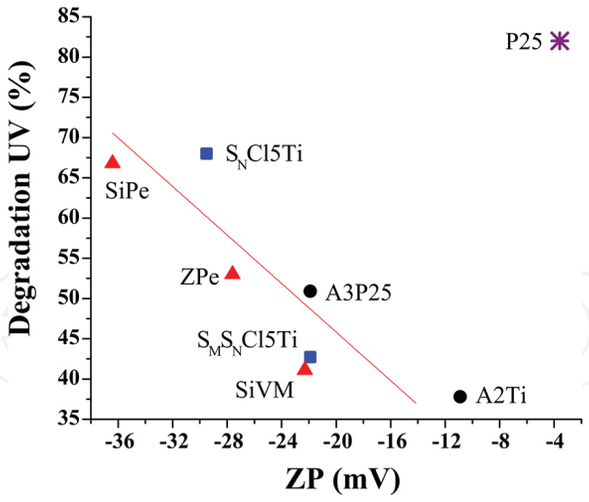

Figure 3. Correlation between degradation RhB under UV radiation and ZP of the better photocatalysts. Spearman's correlations: $r_{Sp} > -0.827$.

According to **Figure 3**, the performance of heterogeneous photocatalysts under UV radiation is related to the zeta potential showing a strong correlation ($r_{Sp} > -0.827$). In the present case, RhB is characterized by its cationic nature, and its compatibility with the photocatalyst surface potential (negative charge) may potentially improve the photocatalyst activity (59). On the other hand, all the photocatalysts exhibited activity higher than that of Degussa P25 under visible radiation, suggesting a potential application of such photocatalysts under sun irradiation. It is important to highlight that S_NCl5Ti is synthesized from silicas nanoparticles, whereas SiPe is prepared from petrochemical waste. Both strategies are viable for the degradation of organic pollutants. Based on the ZP results, we established that photocatalyst dispersions are stable and that the BET and SAXS analyses are in agreement and interrelated with the discussion about the electronic properties of these photocatalysts.

3.4. Energy bandgap (Eg) by DRS

The energy bandgap (E_g) is a relevant parameter for the photocatalytic process because lower values of E_g correspond to less radiation energy required to activate the process, which may reduce the required radiation into the visible light range (60). To determine the photoabsorbance properties, UV-DRS was employed in the wavelength range of 200–800 nm. Table 5 shows E_g of photocatalysts. For comparative reasons data from commercial photocatalyst (P25) were also included.

It was possible to observe strong correlations ($r_{Sp} > -0.749$ and $r_{Sp} > -0.788$) between the energy bandgap (Eg) with pore volume (Vp_{BJH}) and surface area (S_{BET}). Thus, the higher the pore volume, the higher the surface charge (in module), which may promote diffusion of the dye from the solution to the catalyst centers. On the other hand, the higher the surface charge (in module), the lower the energy to promote the electron from the valence band to the conduction band. Comparing the E_g values between the prepared photocatalysts, as shown in Table 5, the E_g of the catalysts ranged from 1.8 to 3.7 eV. Notably, the SiPe sample exhibited the lowest

E_g value among the prepared titania photocatalysts. These results illustrate the role played by E_g on the photocatalytic process and the effects of textural (surface area and pore volume) and electronic (ZP) characteristics.

3.5. Four- and six-membered Silica

Comparing MI systems with nanoparticles and mixed silicas, one can see that systems containing $TiCl_4$ (A1Ti, A2Ti and ATi) and the systems with lower TEOS:$SiCl_4$ ratio (S_NCl5Ti and S_MS_NCl5Ti) afford the lowest %$(SiO)_6$ content (below than 55%). Thus, these materials tend to present more rigid structure of silica represented by four-membered silica ($(SiO)_4$). In the other words, both the presence of P25 and higher TEOS:$SiCl_4$ ratio result in more hydrophilic materials. As a general trend, hydrophilic materials seem to be more easily achieved by a protocol using the synthesis of silica nanoparticles than the MI materials. Although %$(SiO)_6$ was not correlated with degradation of RhB, it is interesting to note that materials with the highest %$(SiO)_6$ content (A3P25 and S_NCl18Ti) afforded better degradation under UV radiation.

3.6. Morphological characteristics obtained using SEM

Scanning electron microscopy (SEM) was used to evaluate the particle morphologies of supports. The low- and high-magnification images of the nanoparticles are shown in **Figure 4**.

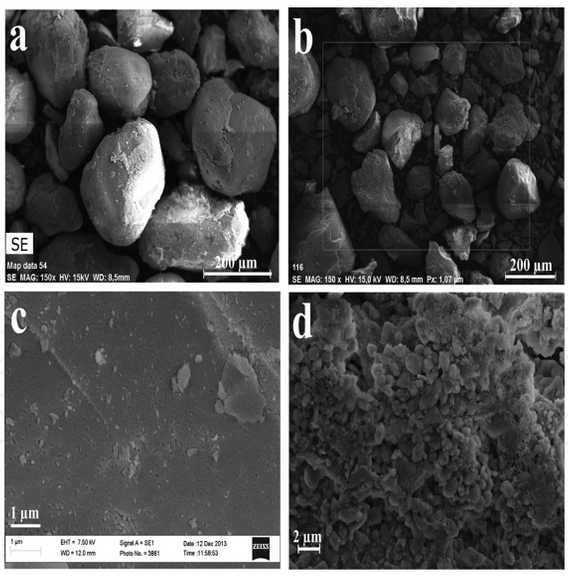

Figure 4. SEM images of (a) SPe, (b) ZPe, (c) of MI materials, (d) S_MS_N5ClTi.

According to **Figure 4a, b** supports SPe and ZPe are larger particles and approximately rounded, whereas synthesized silica supports (S_MS_NCl5Ti) are smaller, amorphous, and aggregate particles (**Figure 4d**). In the case of MI materials, as observed in **Figure 4c**, a large number porous and some particle agglomerates are present on the surface of system. In the

case of MI materials, as observed in **Figure 4c**, a large number porous and some particle agglomerates are present on the surface of system.

4. Conclusions

This work presented three alternative approaches for the degradation of organic pollutants such as RhB. Imprinting molecular materials, synthesized silica particles as catalytic supports from $TiCl_4$ and photocatalysts from industrial and academic waste demonstrated activity for degradation of RhB dye under visible (61.6%) and UV (68%) radiation and are better than the commercial TiO_2 (12.3%) under visible radiation. The textural and structural characteristics of the supported catalyst prepared with fumed silica and petrochemical waste (SiPe), namely the low-energy bandgap (1.8 eV), large surface area (280 $m^2\ g^{-1}$), high pore volume (1.9 $cm^3\ g^{-1}$), and high zeta potential value (−36.4 mV), may have been responsible for their high activity.

Our alternative approaches herein studied could help to overcome the main drawbacks involved in heterogeneous photocatalyst, such as the lack of selectivity, the low surface area, and UV-limited spectrum for commercial samples.

Acknowledgements

This project was partially financed by the Conselho Nacional de Desenvolvimento Científico e Tecnológico (CNPq). Yolice P. Moreno, Cícero C. Escobar and William L. da Silva are grateful for the grant provided by Coordenação de Aperfeiçoamento de Pessoal de Nível Superior (CAPES). The Brazilian Synchrotron Light Laboratory (LNLS, Campinas, Brazil) and the Laboratory of Ion Implantation are thanked for the analysis of the SAXS (Projects D11A-SAXS1-8691 and SAXS1-15911) and RBS, respectively.

Author details

Yolice P. Moreno[1], Cicero C. Escobar[1], William L. da Silva[1] and João H. Z. dos Santos[2*]

*Address all correspondence to: jhzds@iq.ufrgs.br

1 Department of Chemical Engineering - Federal University of Rio Grande do Sul, Rua Engenheiro Luis Englert, CEP Porto Alegre, RS, Brazil

2 Institute of Chemistry - Federal University of Rio Grande do Sul, Av. Bento Gonçalves, CEP Porto Alegre, RS, Brazil

References

[1] Chen J, Liu M, Zhang J, Ying X, Jin L. Photocatalytic degradation of organic wastes by electrochemically assisted TiO_2 photocatalytic system. Journal of Environmental Management. 2004; 70(1): 43–7.

[2] Parolin F, Nascimento UM, Azevedo EB. Microwave-enhanced UV/H_2O_2 degradation of an azo dye (tartrazine): optimization, colour removal, mineralization and ecotoxicity. Environmental Technology. 2013; 34(10): 1247–53.

[3] Ribeiro AR, Nunes OC, Pereira MFR, Silva AMT. An overview on the advanced oxidation processes applied for the treatment of water pollutants defined in the recently launched Directive 2013/39/EU. Environment International. 2015; 75: 33–51.

[4] Andreozzi R, Caprio V, Insola A, Marotta R. Advanced oxidation processes (AOP) for water purification and recovery. Catalysis Today. 1999; 53(1): 51–9.

[5] Nakata K, Fujishima A. TiO_2 photocatalysis: design and applications. Journal of Photochemistry and Photobiology C: Photochemistry Reviews. 2012; 13(3): 169–89.

[6] Shaham-Waldmann N, Paz Y. Modified Photocatalysts. Photocatalysis and Water Purification. Wiley-VCH Verlag GmbH & Co. KGaA; 2013. pp. 103–43.

[7] Ibhadon AO, Fitzpatrick P. Heterogeneous photocatalysis: recent advances and applications. Catalysts. 2013; 3(1): 189–218.

[8] Huang C, Tu Z, Shen X. Molecularly imprinted photocatalyst with a structural analogue of template and its application. Journal of Hazardous Materials. 2013; 248–249(0): 379–86.

[9] Luo X, Deng F, Min L, Luo S, Guo B, Zeng G, et al. Facile one-step synthesis of inorganic-framework molecularly imprinted TiO_2/WO_3 nanocomposite and its molecular recognitive photocatalytic degradation of target contaminant. Environmental Science & Technology. 2013; 47(13): 7404–12.

[10] Lu Z, Huo P, Luo Y, Liu X, Wu D, Gao X, et al. Performance of molecularly imprinted photocatalysts based on fly-ash cenospheres for selective photodegradation of single and ternary antibiotics solution. Journal of Molecular Catalysis A: Chemical. 2013; 378(0): 91–8.

[11] Khraisheh M, Kim J, Campos L, Al-Muhtaseb AaH, Al-Hawari A, Al Ghouti M, et al. Removal of pharmaceutical and personal care products (PPCPs) pollutants from water by novel TiO_2–Coconut Shell Powder (TCNSP) composite. Journal of Industrial and Engineering Chemistry. 2014; 20(3): 979–87.

[12] Yola ML, Eren T, Atar N. A novel efficient photocatalyst based on TiO_2 nanoparticles involved boron enrichment waste for photocatalytic degradation of atrazine. Chemical Engineering Journal. 2014; 250(0): 288–94.

[13] Omri A, Lambert SD, Geens J, Bennour F, Benzina M. Synthesis, surface characterization and photocatalytic activity of TiO_2 supported on almond shell activated carbon. Journal of Materials Science & Technology. 2014; 30(9): 894–902.

[14] Shavisi Y, Sharifnia S, Hosseini SN, Khadivi MA. Application of TiO_2/perlite photocatalysis for degradation of ammonia in wastewater. Journal of Industrial and Engineering Chemistry. 2014; 20(1): 278–83.

[15] Kamaruddin S, Stephan D. Sol–gel mediated coating and characterization of photocatalytic sand and fumed silica for environmental remediation. Water, Air, & Soil Pollution. 2014; 225(5): 1–11.

[16] Wang B, Yang Z, An H, Zhai J, Li Q, Cui H. Photocatalytic activity of Pt–TiO_2 films supported on hydroxylated fly ash cenospheres under visible light. Applied Surface Science. 2015; 324(0): 817–24.

[17] Wickramaratne NP, Jaroniec M. Ordered mesoporous carbon–titania composites and their enhanced photocatalytic properties. Journal of Colloid and Interface Science. 2015; 449(0): 297–303.

[18] Chen X, Liu F, Liu B, Tian L, Hu W, Xia Q. A novel route to graphite-like carbon supporting SnO_2 with high electron transfer and photocatalytic activity. Journal of Hazardous Materials. 2015; 287(0): 126–32.

[19] Cao Z, Yang L, Chen H, Xu C, Qi D, Zhu S, et al. Preparation of Au/TiO_2 nanocomposite particles with high visible-light photocatalytic activity in inverse miniemulsions. Colloid and Polymer Science. 2015; 293(1): 277–88.

[20] da Silva WL, Lansarin MA, Livotto PR, dos Santos JHZ. Photocatalytic degradation of drugs by supported titania-based catalysts produced from petrochemical plant residue. Powder Technology. 2015; 279(0): 166–72.

[21] da Silva WL, Lansarin MA, Stedile FC, dos Santos JHZ. The potential of chemical industrial and academic wastes as a source of supported photocatalysts. Journal of Molecular Catalysis A: Chemical. 2014; 393: 125–33.

[22] da Silva WL, Lansarin MA, dos Santos JHZ. Industrial and agroindustrial wastes: an echotechnological approach to the production of supported photocatalysts. Water Science and Technology. 2016; 73(1): 28–38.

[23] de Escobar CC, Fisch A, dos Santos JHZ. Effect of a sol–gel route on the preparation of silica-based sorbent materials synthesized by molecular imprinting for the adsorption of dyes. Industrial & Engineering Chemistry Research. 2015; 54(1): 254–62.

[24] de Escobar CC, Dallegrave A, Lasarin MA, Zimnoch dos Santos JH. The sol–gel route effect on the preparation of molecularly imprinted silica-based materials for selective and competitive photocatalysis. Colloids and Surfaces A: Physicochemical and Engineering Aspects. 2015; 486: 96–105.

[25] de Escobar CC, Lansarin MA, Zimnoch dos Santos JH. Synthesis of molecularly imprinted photocatalysts containing low TiO_2 loading: evaluation for the degradation of pharmaceuticals. Journal of Hazardous Materials. 2016; 306: 359–66.

[26] de Franco MAE, da Silva WL, Bagnara M, Lansarin MA, dos Santos JHZ. Photocatalytic degradation of nicotine in an aqueous solution using unconventional supported catalysts and commercial ZnO/TiO_2 under ultraviolet radiation. Science of the Total Environment. 2014; 494–495(0): 97–103.

[27] Moreno YP, Cardoso MB, Moncada EA, dos Santos JHZ. Correlating the morphological properties and structural organization of monodisperse spherical silica nanoparticles grown on a commercial silica surface. ChemPhysChem. 2015; 16(14): 2981–94.

[28] Ruiz YPM, Silva WLd, Lansarin MA, Stedile FC, Moncada EA, dos Santos JHZ. Nanoparticles and mixed silicas as supports for the preparation of heterogeneous titania photocatalysts for application in the degradation of rhodamine B dye. In: 18th Brazilian Congress on Catalysis (CBCat); 13–17 September 2015; Porto Seguro. Brazil: CBCat (AJ6H); 2015. p. 1–6.

[29] Fan H-J, Lu C-S, Lee W-LW, Chiou M-R, Chen C-C. Mechanistic pathways differences between P25-TiO_2 and Pt-TiO_2 mediated CV photodegradation. Journal of Hazardous Materials. 2011; 185(1): 227–35.

[30] Whitcombe MJ, Kirsch N, Nicholls IA. Molecular imprinting science and technology: a survey of the literature for the years 2004–2011. Journal of Molecular Recognition. 2014; 27(6): 297–401.

[31] Lofgreen JE, Ozin GA. Controlling morphology and porosity to improve performance of molecularly imprinted sol–gel silica. Chemical Society Reviews. 2014; 43(3): 911–33.

[32] Díaz-García ME, Laínño RB. Molecular imprinting in sol–gel materials: recent developments and applications. Microchimica Acta. 2005; 149(1–2): 19–36.

[33] Walcarius A, Collinson MM. Analytical chemistry with silica sol–gels: traditional routes to new materials for chemical analysis. Annual review of analytical chemistry. 2009; 2: 121–43.

[34] Chen W, Ma Z, Pan X, Hu Z, Dong G, Zhou S, et al. Core@dual–Shell nanoporous SiO_2–TiO_2 composite fibers with high flexibility and its photocatalytic activity. Journal of the American Ceramic Society. 2014; 97(6): 1944–51.

[35] Wang M, Han J, Xiong H, Guo R, Yin Y. Nanostructured hybrid shells of r-GO/AuNP/m-TiO_2 as highly active photocatalysts. ACS Applied Materials & Interfaces. 2015; 7(12): 6909–18.

[36] Li X, Liu D, Song S, Zhang H. Fe_3O_4@SiO_2@TiO_2@Pt hierarchical core–shell microspheres: controlled synthesis, enhanced degradation system, and rapid magnetic separation to recycle. Crystal Growth & Design. 2014; 14(11): 5506–11.

[37] Zhang F, Liu W, Liu Y, Wang J, Ji G. Fabrication and enhanced photocatalytic properties of Pt@SiO_2@TiO_2 composites by surface plasma resonance from Pt nanoparticles. Journal of Nanoparticle Research. 2015; 17(2): 1–9.

[38] de Coelho Escobar C, dos Santos JHZ. Effect of the sol–gel route on the textural characteristics of silica imprinted with Rhodamine B. Journal of Separation Science. 2014; 37(7): 868–75.

[39] Brunauer S, Emmett PH, Teller E. Adsorption of gases in multimolecular layers. Journal of the American Chemical Society. 1938; 60(2): 309–19.

[40] Barrett EP, Joyner LG, Halenda PP. The determination of pore volume and area distributions in porous substances. I. Computations from nitrogen isotherms. Journal of the American Chemical Society. 1951; 73(1): 373–80.

[41] Beaucage G. Approximations leading to a unified exponential/power-law approach to small-angle scattering. Journal of Applied Crystallography. 1995; 28(6): 717–28.

[42] Beaucage G. Small-angle scattering from polymeric mass fractals of arbitrary mass-fractal dimension. Journal of Applied Crystallography. 1996; 29(2): 134–46.

[43] Beaucage G, Kammler HK, Pratsinis SE. Particle size distributions from small-angle scattering using global scattering functions. Journal of Applied Crystallography. 2004; 37(4): 523–35.

[44] Kammler HK, Beaucage G, Kohls DJ, Agashe N, Ilavsky J. Monitoring simultaneously the growth of nanoparticles and aggregates by in situ ultra-small-angle X-ray scattering. Journal of Applied Physics. 2005; 97(5): 054309.

[45] Fidalgo A, Ilharco LM. Chemical tailoring of porous silica xerogels: local structure by vibrational spectroscopy. Chemistry-A European Journal. 2004; 10(2): 392–8.

[46] Fidalgo A, Ciriminna R, Ilharco LM, Pagliaro M. Role of the alkyl-alkoxide precursor on the structure and catalytic properties of hybrid sol–gel catalysts. Chemistry of Materials. 2005; 17(26): 6686–94.

[47] Fidalgo A, Ciriminna R, Lopes L, Pandarus V, Béland F, Ilharco LM, et al. The sol–gel entrapment of noble metals in hybrid silicas: a molecular insight. Chemistry Central Journal. 2013; 7(1): 161.

[48] Fidalgo A, Ilharco LM. Chemical tailoring of porous silica xerogels: local structure by vibrational spectroscopy. Chemistry—A European Journal. 2004; 10(2): 392–8.

[49] Fidalgo A, Ciriminna R, Ilharco LM, Pagliaro M. Role of the alkyl–alkoxide precursor on the structure and catalytic properties of hybrid sol–gel catalysts. Chemistry of Materials. 2005; 17(26): 6686–94.

[50] Zhou W, Fu H. Mesoporous TiO_2: preparation, doping, and as a composite for photocatalysis. ChemCatChem. 2013; 5(4): 885–94.

[51] Ranade VV, Bhandari VM. Industrial wastewater treatment, recycling, and reuse: an overview. Industrial Wastewater Treatment, Recycling and Reuse. 2014; 1–80.

[52] Bayal N, Jeevanandam P. Sol–gel synthesis of SnO_2–MgO nanoparticles and their photocatalytic activity towards methylene blue degradation. Materials Research Bulletin. 2013; 48(10): 3790–9.

[53] Wang M, Song G, Li J, Miao L, Zhang B. Direct hydrothermal synthesis and magnetic property of titanate nanotubes doped magnetic metal ions. Journal of University of Science and Technology Beijing, Mineral, Metallurgy, Material. 2008; 15(5): 644–8.

[54] Sing KSW, Everett DH, Haul RAW, Moscou L, Pierotti RA, Rouquerol J, et al. Reporting physisorption data for gas/solid systems with special reference to the determination of surface area and porosity (Recommendations 1984). Pure and Applied Chemistry. 1985; 57(4): 603–19.

[55] Brinker CJ, Scherer GW. Sol–gel science: the physics and chemistry of sol–gel processing: Access Online via Elsevier; 1990.

[56] Brinker CJ, Frye GC, Hurd AJ, Ashley CS. Fundamentals of sol–gel dip coating. Thin Solid Films. 1991; 201(1): 97–108.

[57] Stoeckel D, Wallacher D, Zickler GA, Perlich J, Tallarek U, Smarsly BM. Coherent analysis of disordered mesoporous adsorbents using small angle X-ray scattering and physisorption experiments. Physical Chemistry Chemical Physics. 2014; 16(14): 6583–92.

[58] Ribeiro PC, Kiminami R, Costa A. Nanosilica synthesized by the Pechini method for potential application as a catalytic support. Ceramics International. 2014; 40(1): 2035–9.

[59] Gaya UI, Abdullah AH. Heterogeneous photocatalytic degradation of organic contaminants over titanium dioxide: a review of fundamentals, progress and problems. Journal of Photochemistry and Photobiology C: Photochemistry Reviews. 2008; 9(1): 1–12.

[60] Gamage McEvoy J, Cui W, Zhang Z. Degradative and disinfective properties of carbon-doped anatase–rutile TiO_2 mixtures under visible light irradiation. Catalysis Today. 2013; 207(0): 191–9.